Article

Insight into the atomic structure of high-voltage spinel LiNi0.5Mn1.5O4 cathode material

Mingxiang Lin, Liubin Ben, Yang Sun, Hao Wang, Zhenzhong Yang, Lin Gu, Xiqian Yu, Xiao-Qing Yang, Haofei Zhao, Richeng Yu, Michel Armand, and Xuejie Huang

Chem. Mater., **Just Accepted Manuscript** • DOI: 10.1021/cm503972a • Publication Date (Web): 04 Dec 2014

Insight into the atomic structure of high-voltage spinel $LiNi_{0.5}Mn_{1.5}O_4$ cathode material in the first cycle

Mingxiang LIN[1,†], Liubin BEN[1,†], Yang SUN[1], Hao WANG[1], Zhenzhong YANG[2], Lin GU[2,*], Xiqian YU[3], Xiao-Qing YANG[3], Haofei ZHAO[2], Richeng YU[2], Michel ARMAND[4] and Xuejie HUANG[1,*]

[1]Key Laboratory for Renewable Energy, Beijing National Laboratory for Condensed Matter Physics, Institute of Physics, Chinese Academy of Sciences, Beijing 100190, China.

[2]Laboratory for Advanced Materials & electron Microscopy, Beijing National Laboratory for Condensed Matter Physics, Institute of Physics, Chinese Academy of Sciences, Beijing 100190, China.

[3]Brookhaven National Laboratory, Upton, NY 11973, USA.

[4]CIC Energigune, Albert Einstein 48, 01510 Miñano, Álava, Spain.

ABSTRACT

Application of high-voltage spinel $LiNi_{0.5}Mn_{1.5}O_4$ cathode material is the closest and the most realistic approach to meeting the mid-term goal of lithium ion batteries for electric vehicles (EVs) and plug-in hybrid electric vehicles (HEVs). This application, however, has been hampered by long-standing issues such as capacity degradation and poor first-cycle coulombic efficiency of $LiNi_{0.5}Mn_{1.5}O_4$ cathode material. Though it is well known that structure of $LiNi_{0.5}Mn_{1.5}O_4$ into which lithium ions are reversibly intercalated plays a critical role in the above issues, structural changes related performance degradation, particularly in the first cycle, are not fully understood. Here we report detailed investigations of local atomic-level and average structure of $LiNi_{0.5}Mn_{1.5}O_4$ during first cycle (3.5-4.9 V) at room temperature. We observed two types of local atomic-level migration of transition metals (TM) ions in the cathode of a well-prepared $LiNi_{0.5}Mn_{1.5}O_4$//Li half-cell during first charge via an aberration-corrected scanning transmission electron microscopy (STEM). Surface regions (~ 2nm) of the cycled $LiNi_{0.5}Mn_{1.5}O_4$ particles show migration of TM ions into lithium tetrahedral sites to form a Mn_3O_4-like structure. Sub-surface regions of the cycled particles, however, exhibit migration of TM ions into empty octahedral sites to form a rocksalt-like structure. The migration of these TM ions are closely related to dissolution of Ni/Mn ions and building-up of charge transfer impedance, which contribute significantly to the capacity degradation and the poor first-cycle coulombic efficiency of spinel $LiNi_{0.5}Mn_{1.5}O_4$ cathode material. Accordingly, we provide suggestions of effective stabilization of $LiNi_{0.5}Mn_{1.5}O_4$ structure to obtain better electrochemical performance.

Keywords: Lithium ion battery, $LiNi_{0.5}Mn_{1.5}O_4$, scanning transmission electron microscopy (STEM), transition metal migration, Mn_3O_4 structure, rocksalt structure.

INTRODUCTION

Lithium ion batteries are one of the most promising energy storage techniques for EVs and HEVs applications.[1, 2] Among many cathode materials for lithium ion batteries, high-voltage spinel $LiNi_{0.5}Mn_{1.5}O_4$ cathode material has attracted much attention due to its intrinsic advantages over current commercial counterparts.[3] Its practical reversible capacity (~136 mAh/g) is comparable to that of commercial $LiCoO_2$, $LiFePO_4$ etc. Its specific energy (~640 wh/kg), however, is higher than many commercial counterparts due to the high operation voltage of ~4.7 V. The additional benefit of the high operating voltage is that the safety of battery packs for EVs and HEVs applications is increased, since fewer cells are needed to achieve the required voltage.[4] Furthermore, the relatively inexpensive Ni and Mn in $LiNi_{0.5}Mn_{1.5}O_4$ make this cathode material particularly desirable for large-scale applications.[5]

Despite the interesting properties and potential applications, spinel $LiNi_{0.5}Mn_{1.5}O_4$ cathode material suffers from several issues that must be overcome before practical application. In particular, it shows significant capacity degradation at high temperature (>60 ^oC) and in full cells employing a graphite as anode.[6] The mechanisms of capacity degradation are not well understood but have been commonly attributed to structural related Mn dissolution,[7-9] or structure-electrolyte related reaction,[10, 11] etc. Another issue that hinders the practical application of this material is its poor first-cycle coulombic efficiency in the first cycle, with a wide range of reported values, e.g. 75-85%.[12, 13] From a practical point of view, such poor and seemly uncontrollable first-cycle coulombic efficiency makes it difficult to balance this cathode with anode (usually graphite) in a full cell.[14] If unbalanced, a full cell may exhibit faster capacity degradation and safety issues, e.g. deposition of lithium on the anode to cause internal short-circuit when a full cell is overcharged.[15, 16] The origin of the poor first-cycle coulombic efficiency is even less understood. None structural related factors such as oxidation of electrolyte,[12, 13, 17-19] inactive conductive carbon,[13] stainless steel positive can,[20] membrane and current collector[21] were all reported to contribute to this issue. Though extensive studies of spinel $LiNi_{0.5}Mn_{1.5}O_4$ cathode material have been performed, its electrochemical performance has only been marginally improved.[3]

Clearly, to further improve the cycling performance of $LiNi_{0.5}Mn_{1.5}O_4$ cathode material, a full understanding of the degradation of the electrochemical performance is essential.

Recently, there has been a significant improvement of the understanding of the role of cathode structure, particularly atomic-level local structure, in lithium intercalation and degradation of electrochemical performance, with the help of advanced electron microscopic techniques.[22-36] Our group recently found that the surface (5-6 nm) of the spinel $LiMn_2O_4$ cathode material decomposes into a Mn_3O_4 structure during charging to 4.3 V.[34] This Mn_3O_4 is directly related to the accelerated speed of Mn dissolution and associated capacity degradation in charged state. For spinel $LiNi_{0.5}Mn_{1.5}O_4$, the average structure, in general, remains stable during electrochemical cycling. However, Kim *et al* reported that TM ions may migrate into other sites in charged state to form new structures, resulting in additional 002 spot observed via TEM selected area electron diffraction (SAED).[37, 38] The nature of such a migration and its influence to the electrochemical performance are not known. It is clear that the migration of TM ions and associated local structure transformations may be critically related to the degradation of electrochemical performance, which is usually difficult to be probed by structural characterization techniques such as XRD.

In this study, spinel $LiNi_{0.5}Mn_{1.5}O_4$ cathode material was investigated by combined local and global structure characterization techniques, e.g. STEM, X-ray absorption spectroscopy (XAS) etc. Such a detailed study, particularly local atomic-level structure study, to the best of our knowledge, has not been performed before. Mechanisms of degradation of electrochemical performance related to the structure of spinel $LiNi_{0.5}Mn_{1.5}O_4$ cathode material are discussed. Furthermore, stabilization of its structure to obtain better electrochemical performance is suggested.

EXPERIMENTAL SECTION

Sample preparation. The $LiNi_{0.5}Mn_{1.5}O_4$ samples were prepared by mixing stiochiometric amounts of Li_2CO_3 (99.9% Alpha Aesar) and $Ni_{0.25}Mn_{0.75}(OH)_2$ (Henan Kelong) and ball milling for 60 minutes.

Samples with the $P4_332$ crystal structure was obtained by placing the mixture in an alumina boat and heating at 900 ^oC for 12h in flow O_2, followed by further annealing at 700 ^oC for 48h in flow O_2.

XRD measurements. XRD patterns were obtained using a Bruker D8 ADVANCE diffractometer with a CuKα radiation source (λ_1 = 1.54056 Å, λ_2 = 1.54439 Å). The diffractometer was equipped with a LYNXEYE detector and operated at 40 kV and 40 mA. Electrochemically cycled cathode samples were taken out of the cell in an argon-filled glove box, and then washed several times in DMC to remove surface electrolyte. After drying in the argon-filled glove box, the cathode samples were sealed in a custom-made air-tight sample holder for XRD. All XRD patterns were refined using the Rietveld method as implemented in the program TOPAS[39].

TEM characterization. TEM characterization was performed using a Philips CM200 electron microscope with a field emission gun, operated at an acceleration voltage of 200 kV. Electrochemically cycled cathode samples were taken out of the cell in an argon-filled glove box, and then washed several times in DMC to remove surface electrolyte. After drying in the argon-filled glove box, the cathode samples were placed on copper grids in the argon-filled glove box. The samples were then transferred to the TEM, without exposure to air, through a custom-made mobile airlock, for bright-field image and SAED pattern collection

Electrode preparation. The $LiNi_{0.5}Mn_{1.5}O_4$ working electrodes for half cell were prepared by spreading the slurry of the active materials (90 wt%), carbon black (5 wt%) and PVdF binder (5 wt%) on Al foil. The electrodes were dried at 100 ^oC in vacuum for 10 h before use. The Swagelok-type half cell was assembled with a lithium metal disk as the counter electrode, and a Celgard polypropylene as the separator saturated with a 1M $LiPF_6$ solution in a mixture of ethylene carbonate (EC) and dimethyl carbonate (DMC) in a 1:1 ratio by volume (LP30) in the argon-filled glove box. The discharge/charge measurements were carried out on a Land BT2000 battery test system (Wuhan, China) at a current rate of C/5 under room temperature (C/5 refers to one Li insertion into $LiNi_{0.5}Mn_{1.5}O_4$ per formula unit in 5 h).

STEM characterization. STEM characterization was performed using a JEM-ARM 200F transmission electron microscope operated at 200 kV. The attainable spatial resolution of the microscope is 80 pm at the incident semi-angle of 25 mrad. The preparation of samples for STEM imaging is similar to that of TEM.

STEM image simulation. All STEM image simulations were based on a fast-Fourier-transform multislice approach[40] and the structure models shown in Figure S2 and S3. The simulated STEM images were performed with uniform parameters, which include an accelerating voltage of 200 kV, beam direction along [110] and a specimen thickness of 50 nm. The simulations with thickness ranging from 20 to 60 nm exhibit no qualitative difference. The incident semi-angle is 25 mrad, acceptance semi-angle is 12-25 mrad, Cs value is 0.001mm and defocus is -0.5 nm.

X-ray Photoelectron Spectroscopy. The X-ray photoelectron spectroscopy (XPS) spectra were recorded with a spectrometer having Mg Kα radiation (ESCALAB 250, Sigma Probe, Thermo VG Scientific Co. Ltd.). All binding energies reported were corrected using the signal for the carbon at 284.8 eV as an internal standard. The peak-fitting and quantitative evaluation was performed with the CasaXPS software. The background was corrected using the Shirley method. The change in manganese valence state at different charged and discharged states were interpreted from the XPS data.

***In-situ* XAS measurements.** *In situ* XAS experiments were carried out at beamline X18A of the National Synchrotron Light Source (NSLS) at Brookhaven National Laboratory in transmission mode using a Si (111) double-crystal monochromator detuned to 35-40% of its original maximum intensity to eliminate the high order harmonics. A reference spectrum of each element was simultaneously collected for energy calibration. X-ray Absorption Near Edge Structure (XANES) data was analyzed with the ATHENA software package.

RESULTS

Electrochemical Performance

The electrochemical performance of spinel $LiNi_{0.5}Mn_{1.5}O_4$ was investigated initially, as shown in Figure 1, before further structural characterization. Figure 1a shows typical charge/discharge curves of a $LiNi_{0.5}Mn_{1.5}O_4$ /Li half cell cycled at room temperature at 0.2 C. The half cell exhibits a first charge capacity of ~147 mAh/g, close to the theoretical value. The first discharge capacity is ~136 mAh/g, similar to that reported in the literature. The coulombic efficiency (discharge capacity/charge capacity) in the first cycle thus is ~92%. After the first cycle, the capacity shows limited degradation with a coulombic efficiency of ~99%, Figure 1b. In addition, the capacity originated from the 4 V plateau is less than 1 mAh/g. PF_6^- intercalation into conductive carbon[13] was also investigated by charging electrodes containing only conductive carbon to 4.9 V. The results indicate that anion intercalation during first charge to high voltage is very limited. In general, the $LiNi_{0.5}Mn_{1.5}O_4$/Li half cell in this study exhibits an excellent electrochemical performance, apart from the non-100% coulombic efficiency in the first cycle. Accordingly, this cathode material with various charge/discharge state (pristine, first charged and first discharged), as indicated in Fig.1a, were selected for further structural characterization.

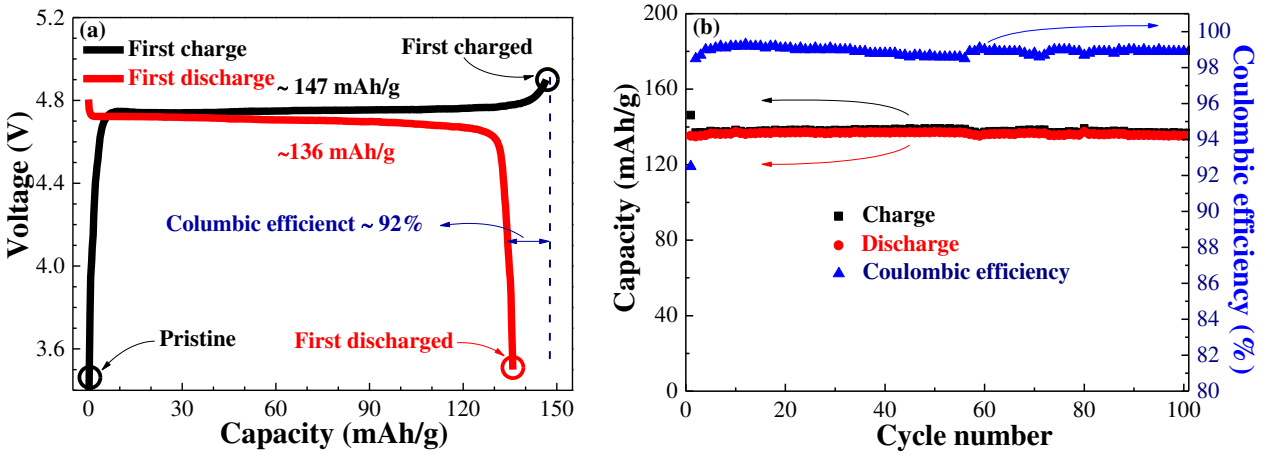

Figure 1. (a) Charge-discharge curves of a typical $LiNi_{0.5}Mn_{1.5}O_4$/Li half-cell in the first cycle; (b) charge-discharge capacities and coulombic efficiency for the first 100 cycles; the circles in (a) indicate the pristine, the first-charged and the first-discharged samples used for further structural characterizations.

Atomic structure of the pristine $LiNi_{0.5}Mn_{1.5}O_4$ particles

The local atomic-level crystal structure of the pristine sample was investigated by STEM as a reference. An extensive number of particles were examined and the results are consistent; thus, only a typical STEM HAADF image is shown in Figure 2. The image shows an atomic-level crystal structure (surface and subsurface) viewed along the [110] crystallographic direction. In this direction, positions of Ni and Mn heavy atomic columns can be clearly identified from a diamond configuration of contrast, Figure 2a (see structure model, Figure 2b). Since the stacking density of the Mn(Ni)-I column is twice that of the Mn(Ni)-II column in this crystallographic direction, the strongest contrast is assigned to the former and the slightly weaker one is assigned to the latter. O atomic column can be identified without difficulty in the HAADF image, Figure. 2a, whereas Li atomic column can hardly be observed due to its small atomic number Z.[41] The STEM HAADF images confirm that the atomic-level surface (Figure 2c) and subsurface regions (Figure 2d) of the pristine sample to be spinel by showing typical arrangement of atoms.[34, 42] In addition, the bulk region of the pristine sample is also spinel, as confirmed by STEM images (supplementary Figure S1a). Relative positions and contrast of Mn(Ni)-I, Mn(Ni)-II and O in the surface and subsurface regions can be better obtained with the help of line profiles as shown in Fig. 2e and 2f, respectively. These positions and associated contrast are consistent with the STEM observations of the spinel structure reported in the literature.[34, 42] There is no strong evidence of contrast caused by impurity phases such as rocksalt in all the STEM images. The large scale image of as-synthesized particles is also shown. (supplementary Figure S2a). TEM SAED results further indicate that the space group of the pristine sample in this study is $P4_332$ by showing typical supperlattice reflections (supplementary Figure S2), consistent with XRD refinement results (supplementary Figure S3a).

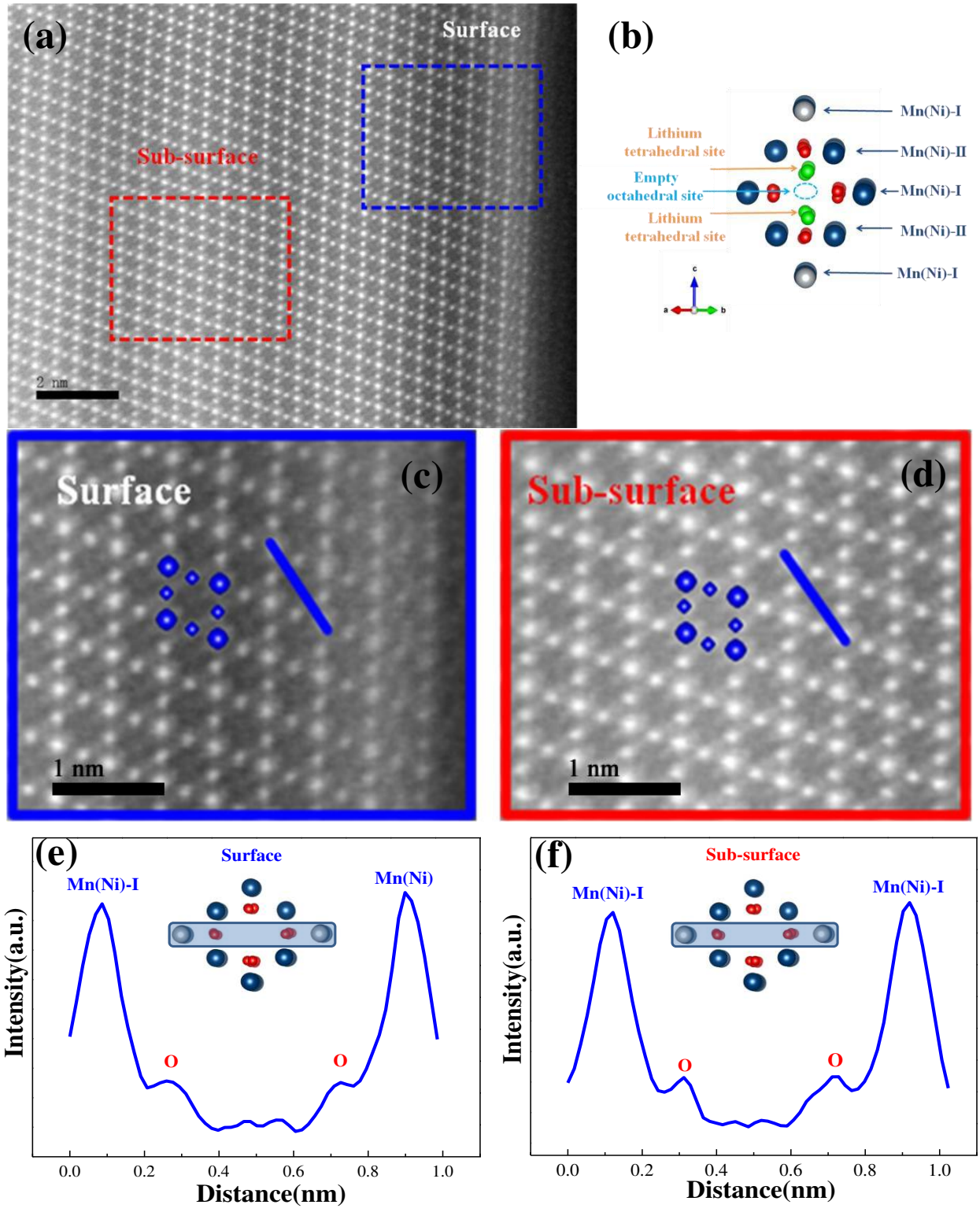

Figure 2. (a) A typical STEM HAADF image of the pristine $LiNi_{0.5}Mn_{1.5}O_4$ sample; (b) a schematic lattice structure of $LiNi_{0.5}Mn_{1.5}O_4$ viewed along the [110] crystallographic direction showing the diamond configuration of arrangement of Mn/Ni atomic columns; (c and d) enlarged regions of the

surface and sub-surface corresponding to the blue and red boxes in (a), respectively; (e and f) line profile corresponding to the blue line in (c) and (d), respectively; schematic lattice structures are overlaid in (c)-(f).

Atomic structure of the charged $LiNi_{0.5}Mn_{1.5}O_4$ particles

After being charged to 4.9 V in the first cycle, majority of the STEM HAADF images obtained from the first-charged sample show the structure to be spinel, which is similar to that of the pristine sample. However, two types of local atomic-level structures different from spinel are clearly observed in the STEM images, Figure 3a.

Close examination of the surface regions, as shown in Figure 3b, clearly reveals the presence of weak contrast in the tetrahedral lithium sites. This contrast cannot be caused by light elements such as Li and O due to their small atomic number Z as discussed above.[41] It can only be attributed to migration of heavy TM ions to the tetrahedral lithium sites during charge. This is somewhat similar to that reported in spinel $LiMn_2O_4$ during charge to 4.3 V, which shows contrast in the lithium tetrahedral sites caused by migration of Mn^{2+} ions to form the Mn_3O_4 structure.[34] For the $LiNi_{0.5}Mn_{1.5}O_4$ sample studied here, probably mainly Ni^{2+} ions migrate into the lithium tetrahedral sites of the spinel structure, as will be discussed later. Notes should be taken that the degree of migration of TM ions into the lithium tetrahedral sites is limited in the first-charged sample. According to the line profile in Figure 3d, the contrast caused by migration of TM ions is only ~26% of that Mn(Ni)-I, indicating that the lithium tetrahedral sites are only partially occupied by TM ions. If these sites were fully occupied by TM ions to from an ideal Mn_3O_4 phase, the contrast ratio would be ~50%, roughly based on atomic packing density along this crystallographic direction (supplementary Figure S4). Notes should also be taken that the Mn_3O_4 structure was formed by almost fully occupation of the lithium tetrahedral sites by Mn^{2+} ions, according to the associated contrast observed.[34]

Detailed investigation of the STEM HAADF image also reveals the definite presence of weak

contrast in the center of the diamond configuration in the sub-surface regions, as shown in Figure 3c. This contrast can be better observed in the line profiles as plotted in Figure. 3e, which is ~8% of that Mn(Ni)-I. According to the crystal structure of spinel viewed along the [110] direction, the center of the diamond configuration is closely related to the empty octahedral sites (see structure model, Figure 2b). Such a contrast is likely be caused by migration of heavy TM ions to the empty octahedral sites. This is similar to that the contrast associated with formation of a rocksalt structure in layered and lithium-rich layered cathode materials during electrochemical cycling.[30, 32, 33] However, for an ideal rocksalt structure, e.g. NiO (Fm-3m), the contrast in the center of the diamond configuration is 100% to the Ni-I, based on atomic packing density along the [110] crystallographic direction (supplementary Figure S5). Thus the migration of TM ions with the formation of the rocksalt-like structure in the sub-surface regions is also very limited. In addition, STEM HAADF images of some isolated bulk regions of the first-charged sample also show migration of TM ions to partially occupy the empty octahedral sites to form the rocksalt-like structure (supplementary Figure S1b). These regions may probably be close to the surface region, which will be discussed later. The large scale of line profile show the homogeneity of Ni/Mn migration after charge (supplementary Figure S1c).

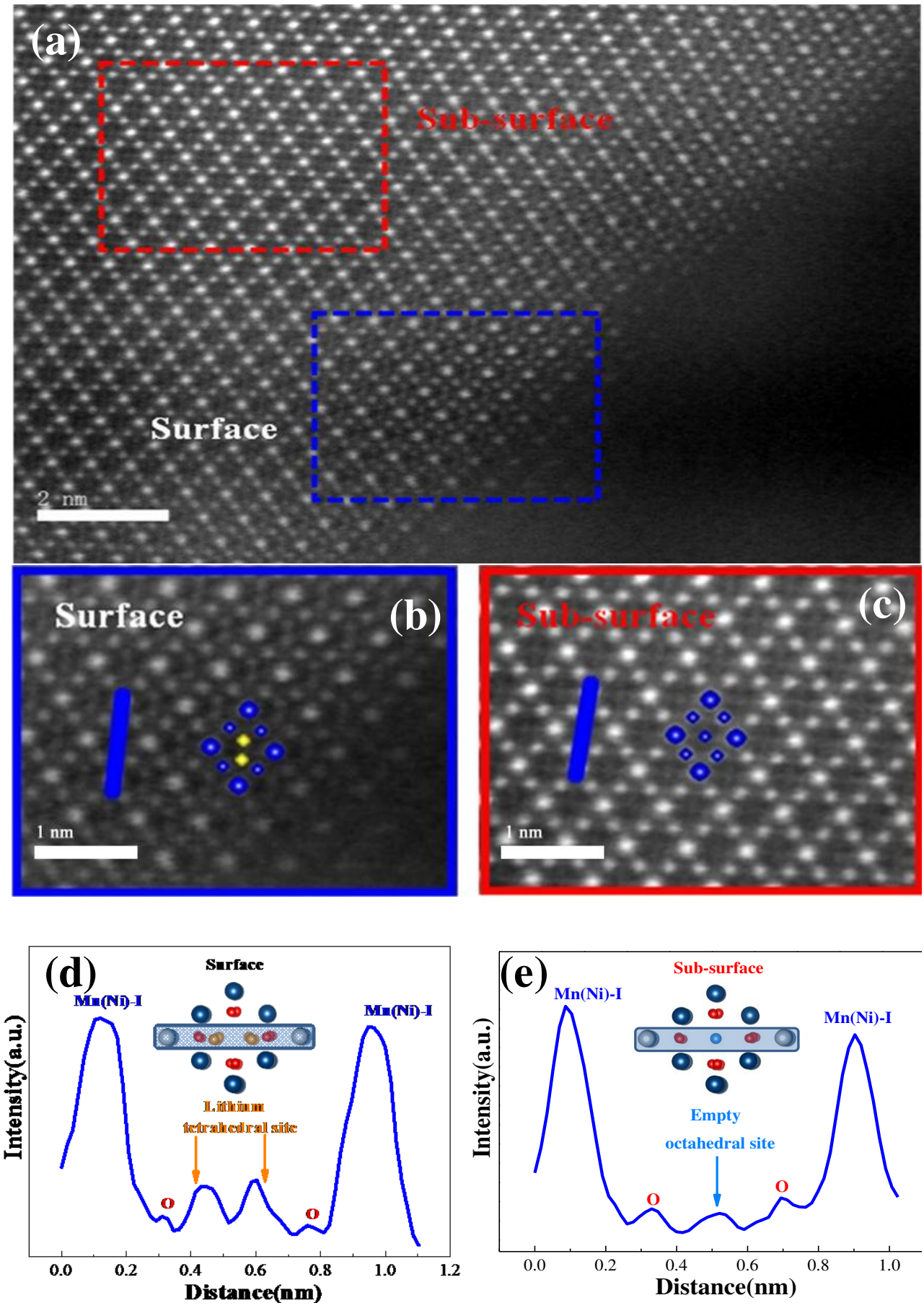
(a)
Sub-surface
Surface
2 nm
Surface
(b)
1 nm
Sub-surface
(c)
1 nm
(d)
Surface
Mn(Ni)-I
Mn(Ni)-I
Lithium
tetrahedral site
O
O
Intensity(a.u.)
0.0
0.2
0.4
0.6
0.8
1.0
1.2
Distance(nm)
(e)
Sub-surface
Mn(Ni)-I
Mn(Ni)-I
Empty
octahedral site
O
O
Intensity(a.u.)
0.0
0.2
0.4
0.6
0.8
1.0
Distance(nm)

Figure 3. (a) A typical STEM image showing the surface and sub-surface regions of the first-charged sample; (b and c) enlarged regions of the surface and sub-surface corresponding to the blue and red boxes in (a), respectively; (d and e) line profile corresponding to the blue lines in (b) and (c), respectively; schematic lattice structures are overlaid in (b)-(e).

Atomic structure of the discharged $LiNi_{0.5}Mn_{1.5}O_4$ particles

After being discharged to 3.5 V, STEM HAADF images of the first-discharged sample show majority of the regions to be spinel, similar to that of the pristine and first-charged samples. However, local structure distortions also present, as shown in Figure 4a. The Mn_3O_4-like and the rocksalt-like structures are present in the surface and sub-surface regions, as can be observed from enlarged regions in Figure 4b and 4c, respectively. Line profiles, Figure 4d and Figure 4e show that the contrast in the lithium tetrahedral sites and empty tetrahedral sites is ~23% and ~10% to that of Mn(Ni)-I, respectively, indicting partial occupation of these sites by TM ions. Some isolated bulk regions of the first-discharged sample also show partial occupation of the empty tetrahedral sites by TM ions (supplementary Figure S1e).

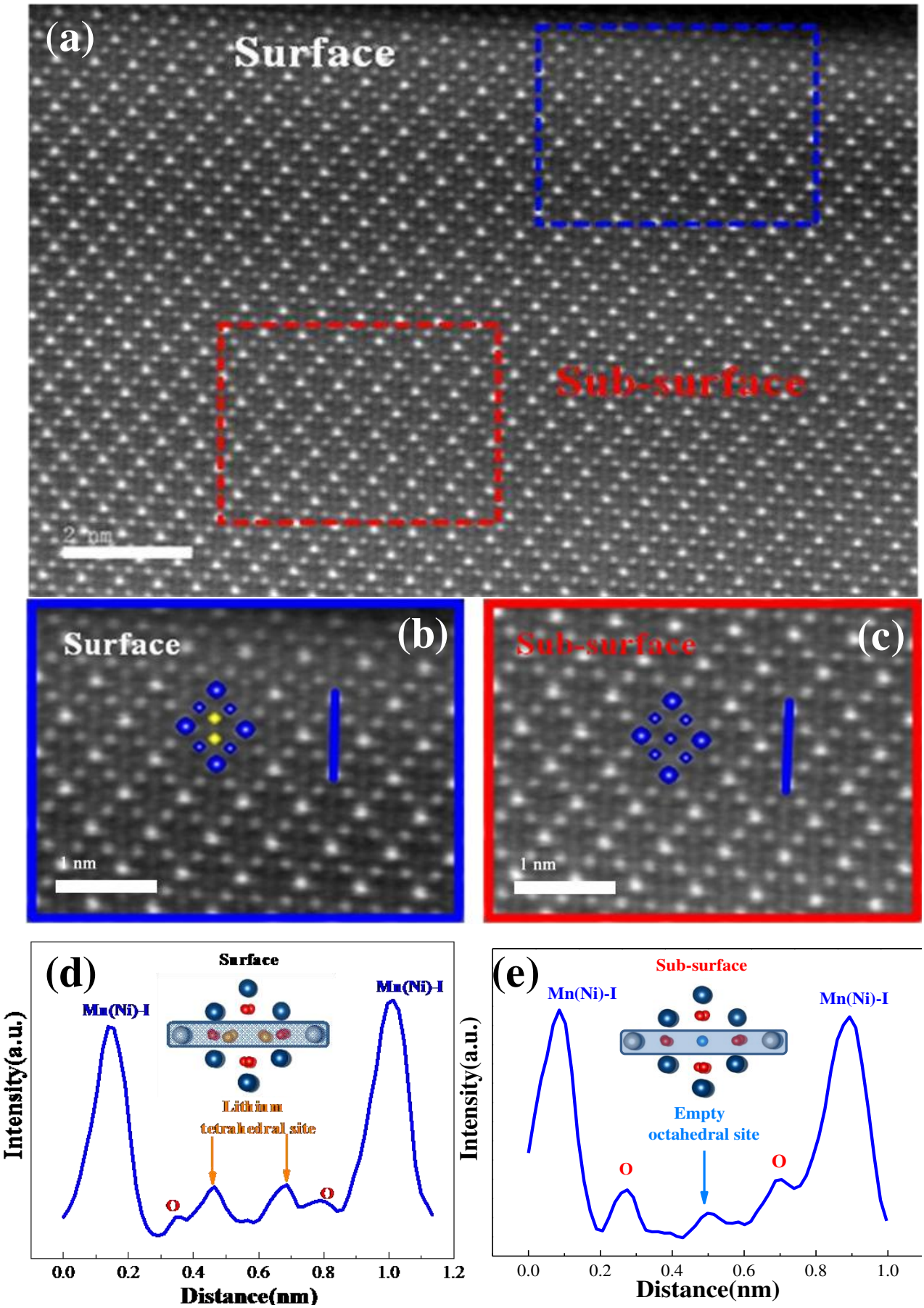
(a)
Surface
Sub-surface
2 nm
Surface
(b)
1 nm
Sub-surface
(c)
1 nm
(d)
Surface
Mn(Ni)-I
Mn(Ni)-I
Lithium
tetrahedral site
O
O
Intensity(a.u.)
0.0
0.2
0.4
0.6
0.8
1.0
1.2
Distance(nm)
(e)
Sub-surface
Mn(Ni)-I
Mn(Ni)-I
Empty
octahedral site
O
O
Intensity(a.u.)
0.0
0.2
0.4
0.6
0.8
1.0
Distance(nm)

Figure 4. (a) A typical STEM image showing the surface and sub-surface regions of the first discharged sample; (b and c) enlarged regions of the surface and sub-surface corresponding to the bulk and red boxes in (a), respectively; (d and e) line profile corresponding to the blue lines in (b) and (c), respectively; schematic lattice structures are overlaid in (b)-(e).

Average crystal structure characterization

The average crystal structure of the electrochemically cycled $LiNi_{0.5}Mn_{1.5}O_4$ samples were investigated by ex-situ XRD and the results are given in the supplementary (Figure S3b and S3c). There is no significant change in the lattice parameters of pristine (a = 8.1692(3) Å) and first-discharged sample (a = 8.1688(2) Å). Enlarged XRD patterns (Figure S3d) further confirms that there is no strong evidence of Mn_3O_4 and NiO phase. Furthermore, structure refinement of all the samples did not show significant improvement in R_{wp}/R_p/goodness of fit factors when occupation of the lithium tetrahedral sites and the empty octahedral sites by TM ions are considered. Thus, in general, the XRD results indicate that the average structure of all samples are spinel, in consistent with the synthesis method and previous ex-situ and in-situ diffraction studies.[38, 43-45]

Electronic structure characterization

The surface electronic structure of the pristine, first-charged and first-discharged cathode material was examined by XPS and the fitted results for Mn are shown in the supplementary (supplementary Figure S6). The results for Ni are not shown due to the traditionally poor quality of XPS data obtained.[46] All samples show typical binding energies of Mn2p1/3 and Mn2p2/3, with a small amount of Mn^{3+} present.[46, 47] There is no strong evidence of the presence of Mn^{2+} ions in all the samples.

The average electronic structure of the $LiNi_{0.5}Mn_{1.5}O_4$ cathode material during electrochemical cycling was also examined by in-situ XAS. The variations of the oxidation states of Ni and Mn in this $LiNi_{0.5}Mn_{1.5}O_4$ cathode material, K-edge XAS spectra were collected respectively at certain states of

charge and discharge, as marked on the first charge/discharge curves in Figure 5. The corresponding X-ray absorption near edge spectroscopy (XANES) results are shown in Figure 5b-5e. In general, there are no obvious differences in the XANES features (edge position and shape) of the pristine and the cycled sample for either Ni or Mn. This indicates the overall reversibility of the structure during electrochemical cycling. K-edge XANES spectra for Ni, shown in Figure 5b and 5c, exhibit rigid shifts of the entire edge toward higher/lower energy sides. The shifts are almost synchronous with the lithium de-intercalation/intercalation process, indicating continuous oxidization/reduction of Ni during charge/discharge. These shifts correspond to an estimated change in Ni-oxidation state from Ni^{2+} in the pristine sample to close to Ni^{4+} in the fully charged sample.[48-50] The difference in Ni-edge energy between the pristine sample (state a) and the first-charged sample (state e) is about 3.5 eV, similar to the comparable values for many Ni-containing spinel and layered cathode material.[51] Although the shape of manganese's XANES spectrum continually changes during charge/discharge, Figure 5d and 5e, the inflection point of its K-edge spectrum stays almost constant at approximately 6556 eV, implying that the oxidation state of Mn may remain close to Mn^{4+} throughout the charge/discharge process.[52] Therefore, the reversible capacity might be attributable solely to the oxidation and reduction of Ni.

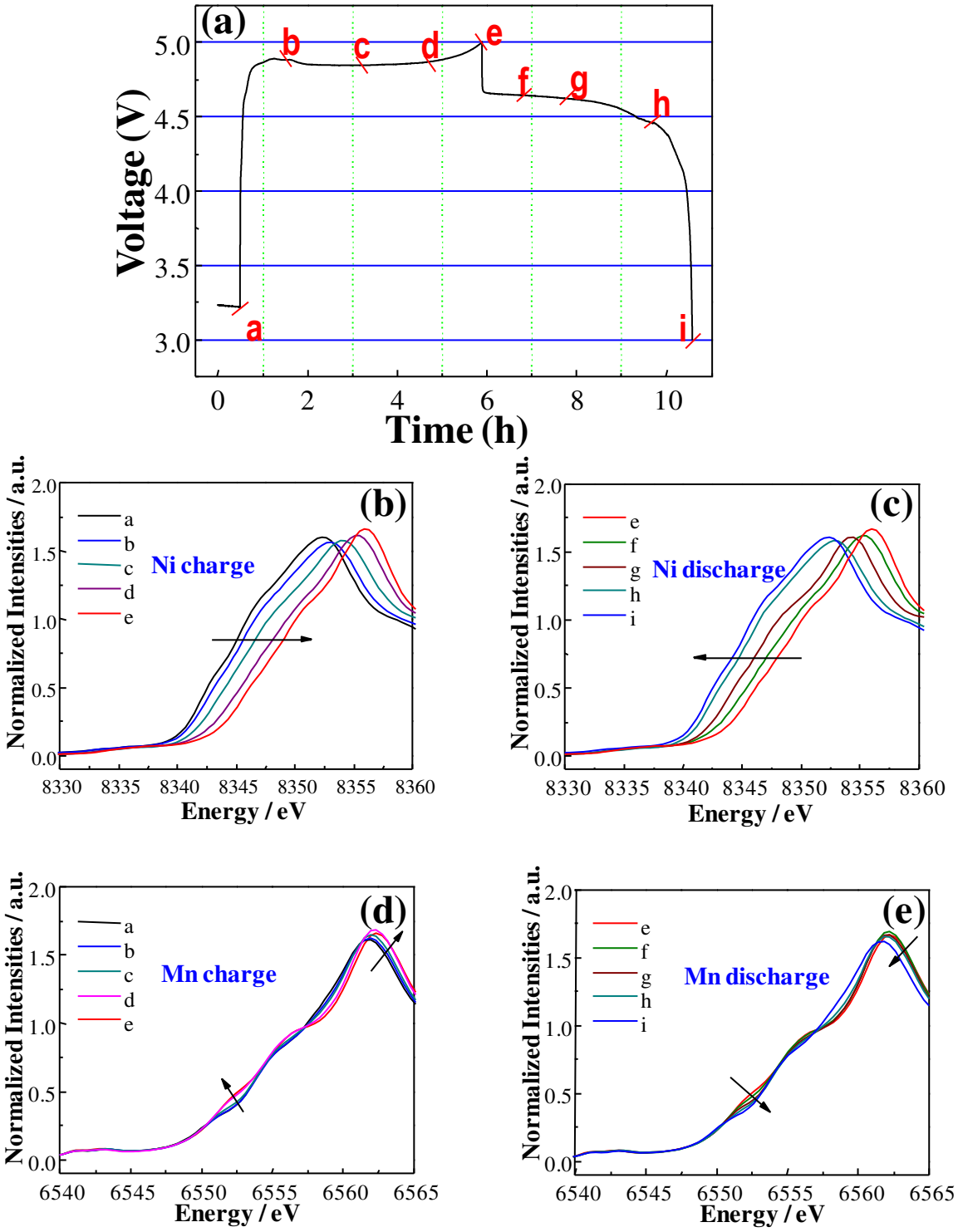

Figure 5. (a) Charge-discharge curves at a rate of 0.2 C for $LiNi_{0.5}Mn_{1.5}O_4$ in the XAS analysis; (b and c) normalized Ni K-edge XANES spectra during the first charge and first discharge, respectively; (d and e) normalized Mn K-edge XANES spectra during the first charge and the first discharge,

respectively; letters of a-i in (a) corresponding to the points in time when XAS data were captured; arrows in (b)-(e) indicate the directions of change of K-edge energy.

DISCUSSION

The above observed average and local atomic-level structure of spinel $LiNi_{0.5}Mn_{1.5}O_4$ cathode material during electrochemical cycling is summarized in Figure 6. The crystal structure, in general, remains stable spinel during electrochemical cycling, based on *ex-situ* XRD results (Figure S2). However, spatially resolved STEM clearly reveals the presence of local structural distortions by migration of TM ions as early as in the first charge to 4.9 V, Figure 3, 4 and Figure S1. After first-charge cycle, the surface regions (~2 nm) of $LiNi_{0.5}Mn_{1.5}O_4$ show partial occupation of the lithium tetrahedral sites by TM ions, which is probably associated with the formation of the Mn_3O_4-like structure, Figure 3b and 4 b. The sub-surface regions and some isolated bulk regions (close to the surface) exhibit partial occupation of the empty octahedral sites by TM ions, which is related to the formation of the rocksalt-like structure, Figure 3c and 4c and Figure S1. Unfortunately due to limit migration of transition metals it is not possible from EDS during STEM imaging to distinguish Ni from Mn based on the EDS results obtained (supplementary Figure S1d). The spinel, Mn_3O_4-like and rocksalt-like structures share the same oxygen close packed framework,[53] indicating the latter two are formed by migration of TM ions within an identical oxygen arrangement. Previously such phase transformations have not been successfully observed possibly due to their appearance in atomic-level regions of several nanometers, thus they are not easily detected by many structural characterizations techniques, e.g. XRD. In addition, for the electronic structure, redox reaction occurs only between Ni^{2+}-Ni^{4+} during cycling, Figure 5, whereas there is a small amount of Mn^{3+} ions but no evidence of Mn^{2+} ions present in all the samples (Figure S6). The electronic structure is generally in agreement with the cycling profile which shows that the capacity is mainly from the 4.7 V plateau and the contribution from the 4 V plateau (Mn^{3+}-Mn^{4+}) is very limited, Figure 1.

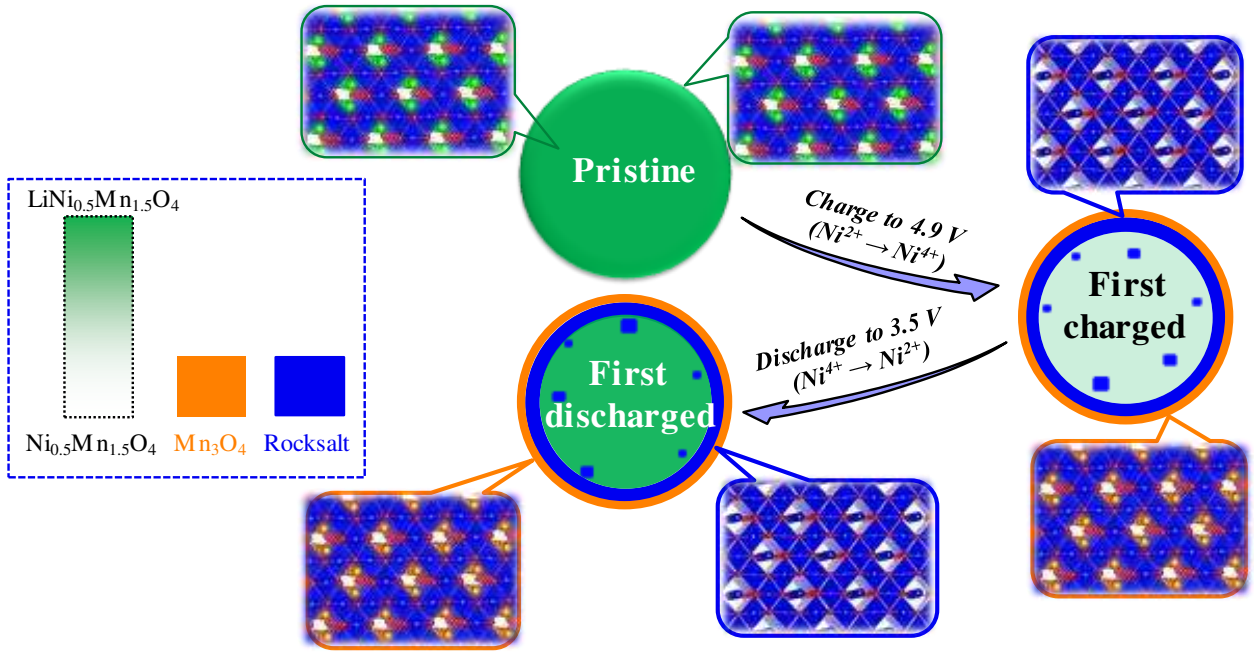

Figure 6. A schematic of migration of TM ions associated with formation of the Mn_3O_4-like and the rocksalt-like structures in spinel $LiNi_{0.5}Mn_{1.5}O_4$ during cycling between 3.5-4.9 V; the lithium concentration of $Li_xNi_{0.5}Mn_{1.5}O_4$ is represented by the transparency of green colour; the fully-transparent green colour indicates $Ni_{0.5}Mn_{1.5}O_4$ (or λ-MnO_2) and the fully-opaque green colour indicates $LiNi_{0.5}Mn_{1.5}O_4$; the Mn_3O_4-like and rocksalt-like structures are indicated by orange and blue colours, respectively; during first charge to 4.9 V, the Mn_3O_4-like structure forms in the ~2 nm surface regions by migration of TM ions to partially occupy the lithium tetrahedral sites; the rocksalt-like structure appears in the sub-surface and some isolated bulk regions (close to the surface) by migration of TM ions to partially occupy the empty octahedral sites; these migrations and associated transformed structures remain during first discharge to 3.5 V. The size of the regions as indicated by colours is not to scale.

Local structural distortions caused by structural destabilization

Destabilisation of $LiNi_{0.5}Mn_{1.5}O_4$ structure accompanied by loss of oxygen during cycling is possibly responsible for the migration of TM ions associated with the formation of the locally distorted

structures. This cathode material as well as many others is highly oxidative and unstable, particularly in the charged (delithiated) stage, as indicated by experimental[30, 32, 34, 54-56] and computational[53, 57-60] studies. Thus, they are prone to migration of TM ions to form more stable structures, accompanied by loss of oxygen. The Mn_3O_4-like structure is similar to that observed in spinel $LiMn_2O_4$ cathode material during charge to 4.3 V.[34] It is likely to be formed by decomposition of delithiated $LiNi_{0.5}Mn_{1.5}O_4$ cathode material and migration of TM ions into the lithium tetrahedral sites, which may be energetically favourable in the delithiated state, as suggested by first-principle calculations of $LiMn_2O_4$.[34] This is also in agreement with previously computer simulation results that migration of TM ions from their octahedral sites to tetrahedral sites have lower migration barrier energy.[58] The appearance of the rocksalt structure is also possibly associated with structural destabilization by migration of TM into the empty octahedral sites and loss of a small amount of oxygen.[26, 28, 29] The oxygen loss involved may suggest that the isolated bulk STEM images (supplementary Figure S1b and S1e) may also be obtained from regions near surface where oxygen is easier to be escaped. Note that though XRD results show all samples to be phase pure, Figure S3, it is argued that the rocksalt structure is always present even in samples annealed in oxygen for a prolonged time. However, all STEM images of pristine sample here do no show strong evidence of the rocksalt-like structure whereas cycled samples shows it appears in a significant amount of regions. This, to some extent, suggests the rocksalt structure may at least increase in its amount after electrochemical cycling, if it also presents in the pristine sample with limited amount. Furthermore, the formation of the rocksalt structure by migration of TM ions into the empty octahedral site confirms for the first time that it grows within the spinel framework. This explains why TEM separate rocksalt and spinel particles are difficult to be observed.[61]

Correlations between electrochemical stability and thermal stability

The migration of TM ions and associated formation of the Mn_3O_4-like and the rocksalt-like

structures can be further understood from thermal-induced structural destabilization of many cathode materials. During heating of spinel $LiNi_{0.5}Mn_{1.5}O_4$ to high temperatures, it decomposes into more thermally stable structures accompanied by loss of a small amount of oxygen, which can be effectively characterized by powder diffraction techniques.[44, 62-64] In particular, Hu *et al* reported that charged spinel $LiNi_{0.5}Mn_{1.5}O_4$ starts to decompose into a $NiMn_2O_4$-type (Mn_3O_4-like) structure below 300 ^oC, accompanied by migration of TM ions into the lithium tetrahedral sites and loss of oxygen.[64] Pasero *et al* found that the pristine spinel $LiNi_{0.5}Mn_{1.5}O_{4-\delta}$ transforms into a rocksalt phase $(Li_{0.333}Mn_{0.5}Ni_{0.167})_xO$ at 950 ^oC with loss of $\delta \sim 0.65$ oxygen.[44] Note that the rocksalt phase with chemical formula of NiO,[65] Li_xNiO[66] was also suggested. In addition, the Mn_3O_4-like and the rocksalt-like structures were also reported in the layered cathode materials during heating to high temperatures. Their structures typically show a layered (R-3m) to Mn_3O_4-type spinel (Fd-3m) and eventually to rocksalt (Fm-3m) phase transformation.[67, 68] This is accompanied by migration of TM ions to the lithium tetrahedral sites (Mn_3O_4) and empty octahedral sites (rocksalt). All these thermal stability studies suggest that the migration of TM ions and associated transformation of structures during heating, to some extent, is similar to that occur during electrochemical cycling. The former usually shows a significant extent of structural change that is relatively easier to be detected by many characterization techniques whereas that latter, in many cases, can only be detected by spatially resolved techniques due to its presence in local atomic-level regions.

Correlations between Mn dissolution and the surface Mn_3O_4-like structure

It is also interesting to compare the surface structure and TM dissolution of $LiNi_{0.5}Mn_{1.5}O_4$ to that of $LiMn_2O_4$ during electrochemical cycling to gain a better understanding of mechanisms of Mn dissolution. Choi *et al* reported that the TM dissolution in $LiNi_{0.5}Mn_{1.5}O_4$ is 0.3% for both Ni and Mn, compared to 3.2% for Mn in $LiMn_2O_4$.[9] This significantly mitigated TM dissolution of $LiNi_{0.5}Mn_{1.5}O_4$ is clearly attributed to the nature and concentration of the Mn_3O_4-like structure, compared to the Mn_3O_4

structure in $LiMn_2O_4$.[34] Our group recently found that the significant amount of surface Mn_3O_4 structure is actually responsible for the Mn dissolution in $LiMn_2O_4$. The Mn_3O_4 structure contains 1/3 soluble Mn^{2+} ions at the tetrahedral site. Once the Mn_3O_4 is formed during the end of charge cycle, the tetrahedral Mn^{2+} ions migrate into the electrolyte in a relatively fast speed during the following discharge cycle. This explains that the reversible appearance/disappearance of the Mn_3O_4 observed is actually related to the formation/dissolution of the tetrahedral Mn^{2+} ions.[34] This is also in agreement with its faster capacity degradation during cycling. However, for $LiNi_{0.5}Mn_{1.5}O_4$, only a small amount of Mn_3O_4-like structure is present in the surface region, suggesting that $LiNi_{0.5}Mn_{1.5}O_4$ is much more structurally stable than $LiMn_2O_4$. More importantly, the lithium tetrahedral sites in the Mn_3O_4-like structure may be mainly occupied by Ni ions since XPS results (Figure S6) does not show strong evidence of Mn^{2+} ions in the surface regions of all the samples. It is known that the solubility of Ni ions is very low in typical EC/DMC electrolyte, compared to that of Mn ions.[7] Once Ni ions are migrated into the lithium tetrahedral sites, they almost remain at these sites. All these result in mitigated dissolution of Mn/Ni and consequently slower capacity degradation of $LiNi_{0.5}Mn_{1.5}O_4$ during electrochemical cycling at room temperature. The occupation of mainly Ni ions at the tetrahedral site is also in agreement with the STEM observation that there is no significant change of the contrast associated with the surface Mn_3O_4-like structure in the cycled samples, Figure 3 b and 4 b. Note that TM dissolution of $LiNi_{0.5}Mn_{1.5}O_4$ is significantly accelerated at high temperature.[7] Its surface structure, particularly the Mn_3O_4-like structure is certainly interesting and is subject to further investigation.

Correlations between electrochemical performance and local structural distortions

The migration of TM ions and associated formation of the Mn_3O_4-like and the rocksalt-like structures in the cathode materials, though occurring in local atomic-level regions, certainly contributes to the degradation of its electrochemical performance.[26, 27, 30, 32-34] The surface Mn_3O_4-like structure contributes to the dissolution of TM ions during cycling, which occurs in a relatively slow speed at

room temperature. This results in gradually loss of active electrode materials. The Mn_3O_4-like as well as the rocksalt-like structures with heavy TM ions on the lithium pathways may lead to building-up of charge transfer impedance.[27, 29, 33] In particular, it is well-known that the empty octahedral sites of spinel $LiNi_{0.5}Mn_{1.5}O_4$ cathode are crucial for lithium ion transportation.[69-71] Occupation of these sites will result in not only slow kinetics of lithium but also inhabitation of occupation of the neighboring lithium site by lithium ions due to electronic repulsion.[72] All these migration of TM ions and associated transformation of structures will result in capacity degradation of cathode materials during electrochemical cycling. Furthermore, the Mn_3O_4-like and the rocksalt-like structures occur as early as in the first-charge cycle, impeding lithium intercalation back into the structure during first-discharge cycle, resulting in poor first-cycle coulombic efficiency. This is in addition to other well-known factors such as oxidation of electrolyte and intercalation of anions during first-cycle. It is also interesting to note that $LiNi_{0.5}Mn_{1.5}O_4$ as well as many other cathode materials may only show significant structure change in the first cycle.[73, 74] After that $LiNi_{0.5}Mn_{1.5}O_4$ structure remains relatively stable and the cathode shows stable electrochemical performance for a very long period. The exact origin behind this is not so clear. It is possible that once the Mn_3O_4-like and rocksalt-like structures are formed in the first cycle, the spinel structure tends to be somewhat stabilized, which only distorts slowly during further cycling at room temperature but may distort quickly when temperature is increased. At elevated temperatures, the locally distorted structures may become nucleation centers for growth of the Mn_3O_4 as well as the rocksalt phases during cycling, resulting in failure of this cathode material.

CONCLUSION

The crystal and the electronic structures of the pristine, the first-charged and the first-discharged high-voltage spinel $LiNi_{0.5}Mn_{1.5}O_4$ cathode material have been characterized by a combination of STEM, XPS, *ex-situ* XRD, *in-situ* XAS etc. These results provide fundamental understanding of the capacity degradation and the poor first-cycle coulombic efficiency in relation to the spinel structure. The

$LiNi_{0.5}Mn_{1.5}O_4$//Li half-cell shows an excellent electrochemical cycling performance, apart from the poor coulombic efficiency in the first cycle, with the average crystal structure to be spinel during electrochemical cycling. However, STEM shows a thin layer of the Mn_3O_4-like structure (~2 nm) formed in the surface regions during first charge to 4.9 V, associated with migration of TM ions to partially occupy the lithium tetrahedral sites. In the sub-surface and some isolated bulk regions (close to surface), STEM results show a rocksalt-like structure occurred during first charge, related to migration of TM ions to partially occupy the empty octahedral sites. The formation of these locally distorted structures and migration of TM ions are attributed to the destabilization and decomposition of spinel $LiNi_{0.5}Mn_{1.5}O_4$ cathode structure and evolution of a small amount of O_2. The surface Mn_3O_4-like structure contributes to the dissolution of TM ions. This structure as well as the rocksalt-like structures with heavy TM ions on the lithium pathways blocks the migration of lithium ions, resulting in building-up of charge transfer impedance and consequently degradation of capacity. Since these structures form as early as in the first charge to 4.9 V, they inevitably contribute to the poor first-cycle coulombic efficiency. Furthermore, these distorted structures though appear in local regions, may become nucleation centers for growth of Mn_3O_4 and rocksalt phases during cycling for prolonged cycles or at high temperatures, leading to failure of the cathode material. Our results suggest that pre-occupation of the lithium tetrahedral sites in the surface of spinel $LiNi_{0.5}Mn_{1.5}O_4$ by a small amount of insoluble ions may possibly be the key to stabilize its structure, to suppress the migration of TM ions and evolution of O_2, thus to improve its electrochemical performance.

ASSOCIATED CONTENT

Supporting information

TEM image and SAED pattern, STEM simulated patterns and line profiles of Mn_3O_4 and NiO rocksalt structures, XRD patterns and Surface XPS results. This material is available free of charge via the Internet at http://pubs.acs.org

AUTHOR INFORMATION

Corresponding author

* Email: xjhuang@iphy.ac.cn (XJ. H) ; l.gu@iphy.ac.cn (L.G)

Author contributions

† Mingxiang Lin and Liubin Ben contribute equally to this work.

Notes

The authors declare no financial interests.

ACKNOWLEDGMENTS

This work was supported by the National Basic Research Program of China (Grant No. 2013CB934002) and the "Strategic Priority Research Program" of the Chinese Academy of Sciences (Grant No. XDA01020304). The work at Brookhaven National Lab was supported by the U.S. Department of Energy, the Assistant Secretary for Energy Efficiency and Renewable Energy, Office of Vehicle Technologies under Contract Number DE-AC02-98CH10886. The authors gratefully acknowledge the technical support of the beamline scientists at X18A (NSLS, BNL).

REFERENCES

1. Tarascon, J. M.; Armand, M. *Nature* **2001,** 414, (6861), 359-367.
2. Armand, M.; Tarascon, J. M. *Nature* **2008,** 451, (7179), 652-657.
3. Manthiram, A.; Chemelewski, K.; Lee, E.-S. *Energy & Environmental Science* **2014,** 7, (4), 1339-1350.
4. Linden D.; T.R., R., *Handbook of batteries. 3rd edition. New York, McGraw-Hill*. 2001.
5. Yan, H. W.; Huang, X. J.; Chen, L. Q. *Journal of Power Sources* **1999,** 81, 647-650.
6. Yoon, T.; Park, S.; Mun, J.; Ryu, J. H.; Choi, W.; Kang, Y. S.; Park, J. H.; Oh, S. M. *Journal of Power Sources* **2012,** 215, 312-316.
7. Pieczonka, N. P. W.; Liu, Z. Y.; Lu, P.; Olson, K. L.; Moote, J.; Powell, B. R.; Kim, J. H. *Journal of Physical Chemistry C* **2013,** 117, (31), 15947-15957.
8. Lu, D.; Xu, M.; Zhou, L.; Garsuch, A.; Lucht, B. L. *J Electrochem Soc* **2013,** 160, (5), A3138-A3143.
9. Choi, W.; Manthiram, A. *J Electrochem Soc* **2006,** 153, (9), A1760-A1764.
10. Aurbach, D.; Markovsky, B.; Talyossef, Y.; Salitra, G.; Kim, H.-J.; Choi, S. *Journal of Power Sources* **2006,** 162, (2), 780-789.
11. Aurbach, D.; Markovsky, B.; Salitra, G.; Markevich, E.; Talyossef, Y.; Koltypin, M.; Nazar, L.; Ellis, B.; Kovacheva, D. *Journal of Power Sources* **2007,** 165, (2), 491-499.
12. Shaju, K. M.; Bruce, P. G. *Dalton Transactions* **2008**, (40), 5471-5475.
13. Xu, W.; Chen, X.; Ding, F.; Xiao, J.; Wang, D.; Pan, A.; Zheng, J.; Li, X. S.; Padmaperuma, A. B.; Zhang, J.-G. *Journal of Power Sources* **2012,** 213, (0), 304-316.
14. Arora, P.; White, R. E.; Doyle, M. *J Electrochem Soc* **1998,** 145, (10), 3647-3667.
15. Arora, P.; Doyle, M.; White, R. E. *J Electrochem Soc* **1999,** 146, (10), 3543-3553.
16. Lu, W.; López, C. M.; Liu, N.; Vaughey, J. T.; Jansen, A.; Dennis W., D. *J Electrochem Soc* **2012,** 159, (5), A566-A570.
17. Goodenough, J. B.; Kim, Y. *Chemistry of Materials* **2010,** 22, (3), 587-603.
18. Brutti, S.; Greco, G.; Reale, P.; Panero, S. *Electrochimica Acta* **2013,** 106, 483-493.
19. Yoon, T.; Kim, D.; Park, K. H.; Park, H.; Jurng, S.; Jang, J.; Ryu, J. H.; Kim, J. J.; Oh, S. M. *J Electrochem Soc* **2014,** 161, (4), A519-A523.
20. Chen, X.; Xu, W.; Xiao, J.; Engelhard, M. H.; Ding, F.; Mei, D.; Hu, D.; Zhang, J.; Zhang, J.-G. *Journal of Power Sources* **2012,** 213, (0), 160-168.
21. Wu, X. W.; Li, X. H.; Wang, Z. X.; Guo, H. J.; Wang, J. X.; Yue, P. *Journal of Solid State Electrochemistry* **2013,** 17, (4), 1029-1038.
22. Devaraju, M. K.; Truong, Q. D.; Honma, I. *RSC Advances* **2013,** 3, (43), 20633.
23. Truong, Q. D.; Devaraju, M. K.; Tomai, T.; Honma, I. *ACS Appl Mater Interfaces* **2013,** 5, (20), 9926-32.
24. Devaraju, M. K.; Truong, Q. D.; Tomai, T.; Hyodo, H.; Sasaki, Y.; Honma, I. *RSC Adv.* **2014,** 4, (94), 52410-52414.
25. Truong, Q. D.; Devaraju, M. K.; Sasaki, Y.; Hyodo, H.; Tomai, T.; Honma, I. *Chemistry of Materials* **2014,** 26, (9), 2770-2773.
26. Gu, M.; Belharouak, I.; Genc, A.; Wang, Z.; Wang, D.; Amine, K.; Gao, F.; Zhou, G.; Thevuthasan, S.; Baer, D. R.; Zhang, J.-G.; Browning, N. D.; Liu, J.; Wang, C. *Nano Lett.* **2012,** 12, (10), 5186-5191.
27. Boulineau, A.; Simonin, L.; Colin, J.-F.; Bourbon, C.; Patoux, S. *Nano Lett.* **2013,** 13, (8), 3857-3863.
28. Wang, R.; He, X. Q.; He, L. H.; Wang, F. W.; Xiao, R. J.; Gu, L.; Li, H.; Chen, L. Q. *Advanced Energy Materials* **2013,** 3, (10), 1358-1367.
29. Zheng, J.; Gu, M.; Xiao, J.; Zuo, P.; Wang, C.; Zhang, J.-G. *Nano Lett.* **2013,** 13, (8), 3824-3830.

30. Hwang, S.; Chang, W.; Kim, S. M.; Su, D.; Kim, D. H.; Lee, J. Y.; Chung, K. Y.; Stach, E. A. *Chemistry of Materials* **2014,** 26, (2), 1084-1092.
31. Jarvis, K. A.; Wang, C.-C.; Manthiram, A.; Ferreira, P. J. *Journal of Materials Chemistry A* **2014,** 2, (5), 1353-1362.
32. Jung, S. K.; Gwon, H.; Hong, J.; Park, K. Y.; Seo, D. H.; Kim, H.; Hyun, J.; Yang, W.; Kang, K. *Advanced Energy Materials* **2014,** 4, (1).
33. Lin, F.; Markus, I. M.; Nordlund, D.; Weng, T. C.; Asta, M. D.; Xin, H. L. L.; Doeff, M. M. *Nature Communications* **2014,** 5.
34. Tang, D.; Sun, Y.; Yang, Z.; Ben, L.; Gu, L.; Huang, X. *Chemistry of Materials* **2014,** 26, (11), 3535-3543.
35. Gu, L.; Zhu, C.; Li, H.; Yu, Y.; Li, C.; Tsukimoto, S.; Maier, J.; Ikuhara, Y. *Journal of the American Chemical Society* **2011,** 133, (13), 4661-4663.
36. Wang, Y.-Q.; Gu, L.; Guo, Y.-G.; Li, H.; He, X.-Q.; Tsukimoto, S.; Ikuhara, Y.; Wan, L.-J. *Journal of the American Chemical Society* **2012,** 134, (18), 7874-7879.
37. Kim, J. H.; Myung, S. T.; Yoon, C. S.; Kang, S. G.; Sun, Y. K. *Chemistry of Materials* **2004,** 16, (5), 906-914.
38. Kim, J.-H.; Yoon, C. S.; Myung, S.-T.; Prakash, J.; Sun, Y.-K. *Electrochemical and Solid-State Letters* **2004,** 7, (7), A216-A220.
39. *Bruker A X S 2008 TOPAS V4: General Profile and Structure Analysis Software for Powder Diffraction Data.- User's Manual [Karlsruhe: Bruker AXS]*
40. Ishizuka, K. *Ultramicroscopy* **2002,** 90, (2–3), 71-83.
41. Findlay, S. D.; Shibata, N.; Sawada, H.; Okunishi, E.; Kondo, Y.; Ikuhara, Y. *Ultramicroscopy* **2010,** 110, (7), 903-923.
42. Huang, R.; Ikuhara, Y. H.; Mizoguchi, T.; Findlay, S. D.; Kuwabara, A.; Fisher, C. A. J.; Moriwake, H.; Oki, H.; Hirayama, T.; Ikuhara, Y. *Angewandte Chemie International Edition* **2011,** 50, (13), 3053-3057.
43. Idemoto, Y.; Sekine, H.; Ui, K.; Koura, N. *Solid State Ionics* **2005,** 176, (3–4), 299-306.
44. Pasero, D.; Reeves, N.; Pralong, V.; West, A. R. *J Electrochem Soc* **2008,** 155, (4), A282-A291.
45. Rhodes, K.; Meisner, R.; Kim, Y.; Dudney, N.; Daniel, C. *J Electrochem Soc* **2011,** 158, (8), A890-A897.
46. Yan, G.; Li, X.; Wang, Z.; Guo, H.; Xiong, X. *Journal of Power Sources* **2014,** 263, 231-238.
47. Mo, M.; Hui, K. S.; Hong, X.; Guo, J.; Ye, C.; Li, A.; Hu, N.; Huang, Z.; Jiang, J.; Liang, J.; Chen, H. *Applied Surface Science* **2014,** 290, 412-418.
48. Mukerjee, S.; Yang, X. Q.; Sun, X.; Lee, S. J.; McBreen, J.; Ein-Eli, Y. *Electrochimica Acta* **2004,** 49, (20), 3373-3382.
49. Lafont, U.; Locati, C.; Borghols, W. J. H.; Łasińska, A.; Dygas, J.; Chadwick, A. V.; Kelder, E. M. *Journal of Power Sources* **2009,** 189, (1), 179-184.
50. Kawaura, H.; Takamatsu, D.; Mori, S.; Orikasa, Y.; Sugaya, H.; Murayama, H.; Nakanishi, K.; Tanida, H.; Koyama, Y.; Arai, H.; Uchimoto, Y.; Ogumi, Z. *Journal of Power Sources* **2014,** 245, 816-821.
51. Yu, X.; Lyu, Y.; Gu, L.; Wu, H.; Bak, S.-M.; Zhou, Y.; Amine, K.; Ehrlich, S. N.; Li, H.; Nam, K.-W.; Yang, X.-Q. *Advanced Energy Materials* **2013**.
52. Yoon, W.-S.; Balasubramanian, M.; Chung, K. Y.; Yang, X.-Q.; McBreen, J.; Grey, C. P.; Fischer, D. A. *Journal of the American Chemical Society* **2005,** 127, (49), 17479-17487.
53. Wang, L.; Maxisch, T.; Ceder, G. *Chemistry of Materials* **2006,** 19, (3), 543-552.
54. Chiang, Y.-M.; Wang, H.; Jang, Y.-I. *Chemistry of Materials* **2000,** 13, (1), 53-63.
55. Yabuuchi, N.; Kim, Y.-T.; Li, H. H.; Shao-Horn, Y. *Chemistry of Materials* **2008,** 20, (15), 4936-4951.
56. Wu, L.; Nam, K.-W.; Wang, X.; Zhou, Y.; Zheng, J.-C.; Yang, X.-Q.; Zhu, Y. *Chemistry of*

Materials **2011,** 23, (17), 3953-3960.
57. Reed, J.; Ceder, G.; Van Der Ven , A. *Electrochemical and Solid-State Letters* **2001,** 4, (6), A78-A81.
58. Reed, J.; Ceder, G. *Chemical Reviews* **2004,** 104, (10), 4513-4534.
59. Bhattacharya, J.; Wolverton, C. *Physical Chemistry Chemical Physics* **2013,** 15, (17), 6486-6498.
60. Kishida, I.; Orita, K.; Nakamura, A.; Yokogawa, Y. *Journal of Power Sources* **2013,** 241, (0), 1-5.
61. Wang, L. P.; Li, H.; Huang, X. J.; Baudrin, E. *Solid State Ionics* **2011,** 193, (1), 32-38.
62. Song, J.; Shin, D. W.; Lu, Y.; Amos, C. D.; Manthiram, A.; Goodenough, J. B. *Chemistry of Materials* **2012,** 24, (15), 3101-3109.
63. Cai, L.; Liu, Z. C.; An, K.; Liang, C. D. *Journal of Materials Chemistry A* **2013,** 1, (23), 6908-6914.
64. Hu, E.; Bak, S.-M.; Liu, J.; Yu, X.; Zhou, Y.; Ehrlich, S. N.; Yang, X.-Q.; Nam, K.-W. *Chemistry of Materials* **2013,** 26, (2), 1108-1118.
65. Amine, K.; Tukamoto, H.; Yasuda, H.; Fujita, Y. *Journal of Power Sources* **1997,** 68, (2), 604-608.
66. Zhong, Q.; Bonakdarpour, A.; Zhang, M.; Gao, Y.; Dahn, J. R. *J Electrochem Soc* **1997,** 144, (1), 205-213.
67. Bak, S.-M.; Nam, K.-W.; Chang, W.; Yu, X.; Hu, E.; Hwang, S.; Stach, E. A.; Kim, K.-B.; Chung, K. Y.; Yang, X.-Q. *Chemistry of Materials* **2013,** 25, (3), 337-351.
68. Nam, K.-W.; Bak, S.-M.; Hu, E.; Yu, X.; Zhou, Y.; Wang, X.; Wu, L.; Zhu, Y.; Chung, K.-Y.; Yang, X.-Q. *Adv Funct Mater* **2013,** 23, (8), 1047-1063.
69. Thackeray, M. M.; Johnson, P. J.; Depicciotto, L. A.; Bruce, P. G.; Goodenough, J. B. *Materials Research Bulletin* **1984,** 19, (2), 179-187.
70. Ma, X. H.; Kang, B.; Ceder, G. *J Electrochem Soc* **2010,** 157, (8), A925-A931.
71. Xu, B.; Meng, S. *Journal of Power Sources* **2010,** 195, (15), 4971-4976.
72. Thackeray, M. M.; David, W. I. F.; Bruce, P. G.; Goodenough, J. B. *Materials Research Bulletin* **1983,** 18, (4), 461-472.
73. Johnson, C. S.; Li, N. C.; Lefief, C.; Vaughey, J. T.; Thackeray, M. M. *Chemistry of Materials* **2008,** 20, (19), 6095-6106.
74. Yabuuchi, N.; Yoshii, K.; Myung, S. T.; Nakai, I.; Komaba, S. *Journal of the American Chemical Society* **2011,** 133, (12), 4404-4419.

TABLE OF CONTENT